RAA 2019 Vol. **19** No. **6**, 84(10pp) doi: 10.1088/1674–4527/19/6/84

http://www.raa-journal.org *http://iopscience.iop.org/raa*

Research in Astronomy and Astrophysics

Can an injection model replenish filaments in a weak magnetic environment?

Peng Zou[1,2], Chao-Wei Jiang[1], Feng-Si Wei[1] and Wen-Da Cao[3]

[1] Institute of Space Science and Applied Technology, Harbin Institute of Technology, Shenzhen 518055, China; *awaken@hit.edu.cn*

[2] School of Astronomy & Space Science, Nanjing University, Nanjing 210023, China

[3] Big Bear Solar Observatory, New Jersey Institute of Technology, 40386 North Shore Lane, Big Bear City, CA 92314, USA

Received 2018 October 9; accepted 2018 December 19

Abstract We observed an Hα surge that occurred in NOAA Active Region 12401 on 2015 August 17, and we discuss its trigger mechanism, and kinematic and thermal properties. It is suggested that this surge was caused by a chromospheric reconnection which ejected cool and dense material with transverse velocity of about 21–28 km s^{-1} and initial Doppler velocity of 12 km s^{-1}. This surge is similar to the injection of newly formed filament materials from their footpoints, except that the surge here occurred in a relatively weak magnetic environment of $\sim$100 G. Thus, we discuss the possibility of filament material replenishment via the erupting mass in such a weak magnetic field, which is often associated with quiescent filaments. It is found that the local plasma can be heated up to about 1.3 times the original temperature, which results in an acceleration of about –0.017 km s^{-2}. It can lift the dense material up to 10 Mm and higher with an inclination angle smaller than 50°, namely the typical height of active region filaments, but it can hardly inject the material up to those filaments higher than 25 Mm, like some quiescent filaments. Thus, we think that the injection model does not work well in describing the formation of quiescent filaments.

Key words: Sun: activity — Sun: chromosphere — Sun: filaments, prominences

1 INTRODUCTION

Solar filaments are heavy and cold objects in the Sun's hot corona and they are closely related with solar eruptions such as coronal mass ejections (Chen 2011). It is commonly believed that filaments are sustained by special magnetic configurations, including magnetic flux ropes or sheared magnetic arches with dips (Kippenhahn & Schlüter 1957; Kuperus & Raadu 1974). Their formation process has been discussed by many authors (van Ballegooijen & Martens 1989; Rust & Kumar 1994; Li & Zhang 2016; Xia et al. 2014; Xia & Keppens 2016; Song et al. 2017). Three models for replenishing the filament materials are widely accepted, the magnetic flux rope lifting model (Rust & Kumar 1994; Deng et al. 2000; Okamoto et al. 2008; Leake & Linton 2013), the evaporation and condensation model (Mok et al. 1990; Antiochos & Klimchuk 1991; Dahlburg et al. 1998) and the cool material injection model (Chae 2003; Liu et al. 2005; Zou et al. 2016, 2017). The injection model, which follows the scenario that cool and dense chromosphere materials inject into the filament channel via a chromospheric magnetic reconnection, was first observed and proposed by Chae (2003). From their observation, Liu et al. (2005) suggested that erupting Hα surges may be directly linked to the replenishment of filament materials. Furthermore, more and more observational evidence supports this scenario (Zou et al. 2016, 2017; Wang et al. 2018). All of these works indicate that a chromospheric eruption can be a source of filament replenishment.

Fan-like Hα surges, which are recognized as chromospheric eruptions, have been reported by several authors in the past few decades (Roy 1973; Asai et al. 2001; Shimizu et al. 2009; Robustini et al. 2016; Li et al. 2016; Hou et al. 2016; Yang et al. 2016; Robustini et al. 2018). Most of them are observed above the light bridges of sunspots (Roy 1973; Asai et al. 2001; Shimizu et al. 2009; Hou et al. 2016; Robustini et al. 2016; Yang et al. 2016; Robustini et al. 2018). They can last for several hours or even one day. During the period, they can be recurrent and exhibit a wall-like appearance (Yang et al. 2016). The speed of their eruption can reach 100 – 200 km s^{-1} (Robustini et al. 2016). The eruptions are accompanied with strong inten-

sity enhancements that can be observed in footpoints of surges using a chromospheric line. Since they are located in polarity inversion lines (PILs) with high current density, these brightenings are thought to be indicators of magnetic reconnection (Shimizu et al. 2009). The magnetic reconnection can lift the dense plasma up into the corona by magnetic tension force, a process which was simulated by Jiang et al. (2011).

Few papers have discussed comparison between simulations and observations that replenish filament material via an injection model (Zou et al. 2016, 2017). The study by Zou et al. (2017) identified extreme brightenings observed in Hα images and the co-spatial brightenings in C II and Si IV observed by the *Interface Region Imaging Spectrograph* (*IRIS*). Both of these studies indicate that violet heating occurred. Replenishment of the material, that is associated with the eruptive velocity of filament fibrils, is possible. In contrast, the study by Zou et al. (2016) showed that the bright points in Hα are weak and the transverse velocity of fibrils are small, namely 5 – 10 km s^{-1}. It seems the plasma can hardly replenish the filament. However, the filament was forming. It is noted that the observations of filament formation via injection process are all active region filaments and intermediate filaments (Chae 2003; Zou et al. 2016, 2017; Wang et al. 2018), which have low magnetic configuration. Thus, an interesting question is: can the injection model also work in a weak magnetic environment to replenish the materials for quiescent filaments?

In this paper, we report an observation by the Fast Imaging Solar Spectrograph (FISS, Chae et al. 2013), attached to the Goode Solar Telescope (GST, Cao et al. 2010; Goode & Cao 2012) at Big Bear Solar Observatory (BBSO), of a fan-like Hα surge caused by weak parasitic magnetic field emergence, which may be able to shed some light on this question.

2 OBSERVATIONS

The fan-like surge occurred in NOAA Active Region 12401 on 2015 August 17. The field of view (FOV) of FISS is shown in Figure 1 using a white quadrangle. This eruption was clearly observed by FISS in Hα and Ca II spectral lines. FISS is an imaging spectrograph mounted on GST. It adopts an Echelle disperser with field scanning method. Two spectral bands (Hα and Ca II 8542 Å) are available simultaneously in two-dimensional spectra and images. The FISS can provide reconstructed images of the photosphere to chromosphere. This can help us to understand the physical processes associated with various phenomenons, such as spicules, prominences and chromospheric eruptions, in multiple layers. The FOV of reconstructed images is $40'' \times 40''$. It is $40''$ in the slit direction by 250 steps in the scanning direction. The spatial resolution is $0.16''$, the cadence is 43 s for both lines and the spectral resolution is 0.0168 Å per pixel for Hα and 0.0161 Å per pixel for Ca II 8542 Å. To understand the underlying mechanism of this surge, we obtain the magnetograms taken by the Helioseismic and Magnetic Imager (HMI, Scherrer et al. 2012; Schou et al. 2012) on board *Solar Dynamics Observatory* (*SDO*). The magnetogram has a spatial resolution of $0.5''$ and a cadence of 45 s. For co-aligning the images recorded by different instruments, the reconstructed images of the Hα line wings are compared with the continuum of HMI/*SDO*. For a comparison with the chromospheric images, the 1600 Å images acquired by the Atmospheric Imaging Assembly (AIA, Lemen et al. 2012) are employed in our work.

Table 1 Increases of Source Function and Temperature Derived from Fitting

Point No.	Increased Rate	Increased Temperature (K)
P1	0.44 – 0.82	850 – 2775
P2	0.52 – 0.90	950 – 3000
P3	0.38 – 0.76	760 – 2560
P4	0.40 – 0.77	780 – 2610
P5	0.62 – 1.05	1170 – 3480

3 RESULTS

Our observation period is from 16:22 UT to 18:00 UT. However, because of rotation in the FOV, we cannot observe the footpoints of this surge after 17:39 UT. This surge began a little earlier than our observation, thus the initial eruption was already occurring. After the first eruption, nearby plasmas start brightening and some dark fibrils are elongated from the brightenings. Initially, the brightenings are isolated and intermittent. After 16:45 UT, the brightenings form a ribbon and dark plasma current associated the brightenings. We display some newly erupted fibrils at different times in the middle row of Figure 2 using Hα –0.5 Å. The Doppler velocity maps, evaluated by the bisector method, indicate that the dark fibrils connected to the brightenings are erupting plasma (see the bottom row of Fig. 2). The attached Hα movie (`http://www.raa-journal.org/docs/Supp/ms4310halpha_movie.mpg`) shows the full evolution of the observation period. It is noted that the intensity enhancement of bright points is extremely strong, which is roughly 1.5 or even 2 times the quiescent area. By contrast, the eruptive fibrils are absorptive in both chromospheric lines and extreme ultraviolet (EUV) (see Fig. 1).

3.1 Evolution of Magnetic Fields

In order to know whether this is a reconnection-triggered eruption, we also display the magnetograms above the Hα

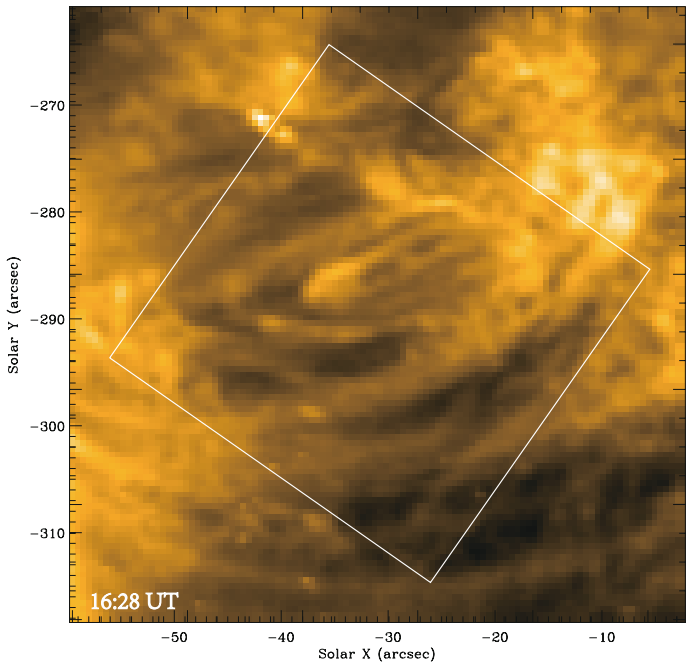

Fig. 1 Figure displays the 171 Å image at 16:28 UT and the *white quadrangle* marks the FOV of FISS/GST.

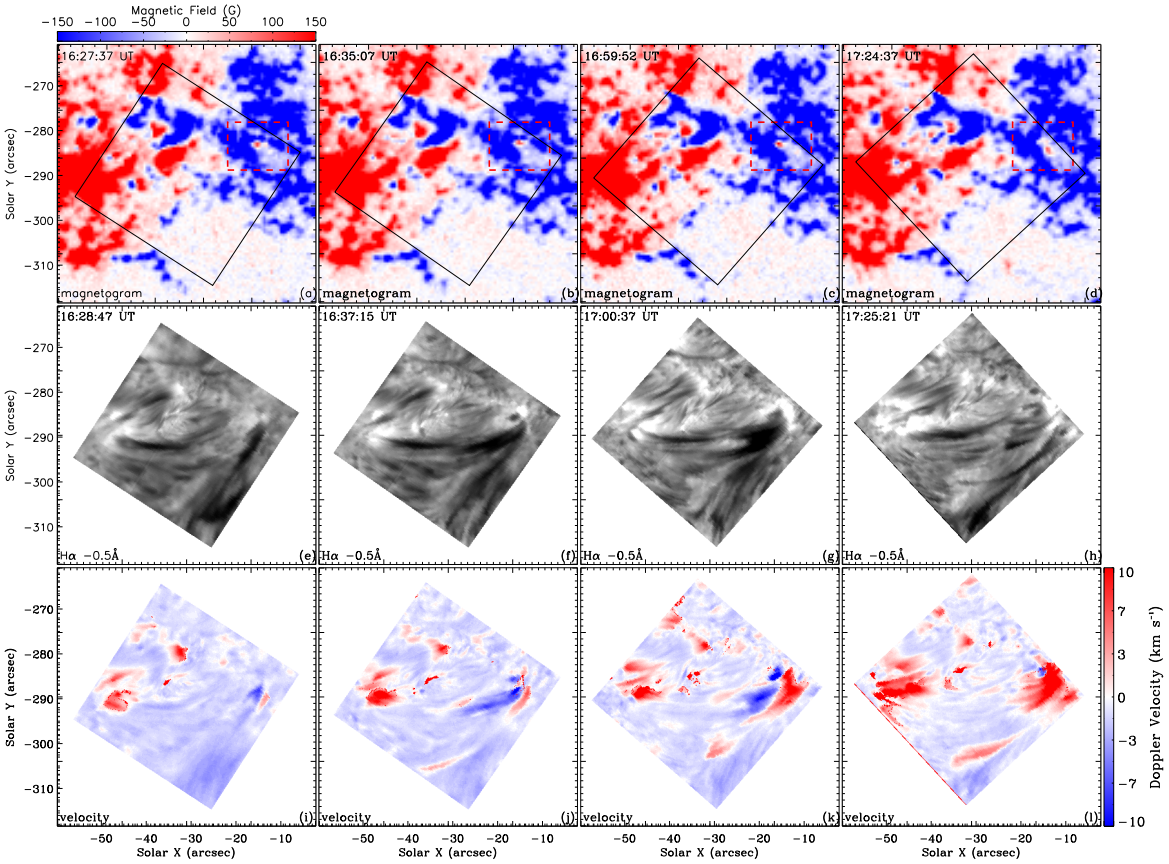

Fig. 2 This figure exhibits the magnetograms (*upper row*), Hα –0.5 Å images (*middle row*) and Doppler velocity maps (*bottom row*). The *black quadrangles* in magnetograms indicate the FOV of FISS/GST and the *red dashed boxes* in the first row are the areas for calculating the positive magnetic flux evolution.

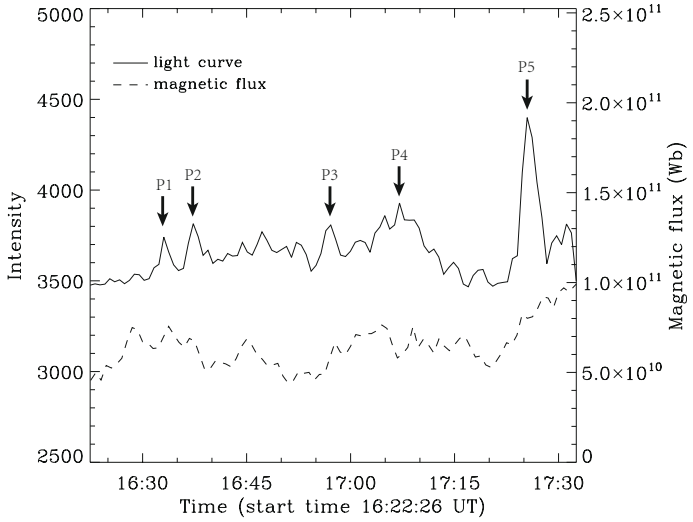

Fig. 3 The light curve of brightenings observed in the Hα line center (*black solid line*) and positive magnetic flux in the same area (*black dashed line*).

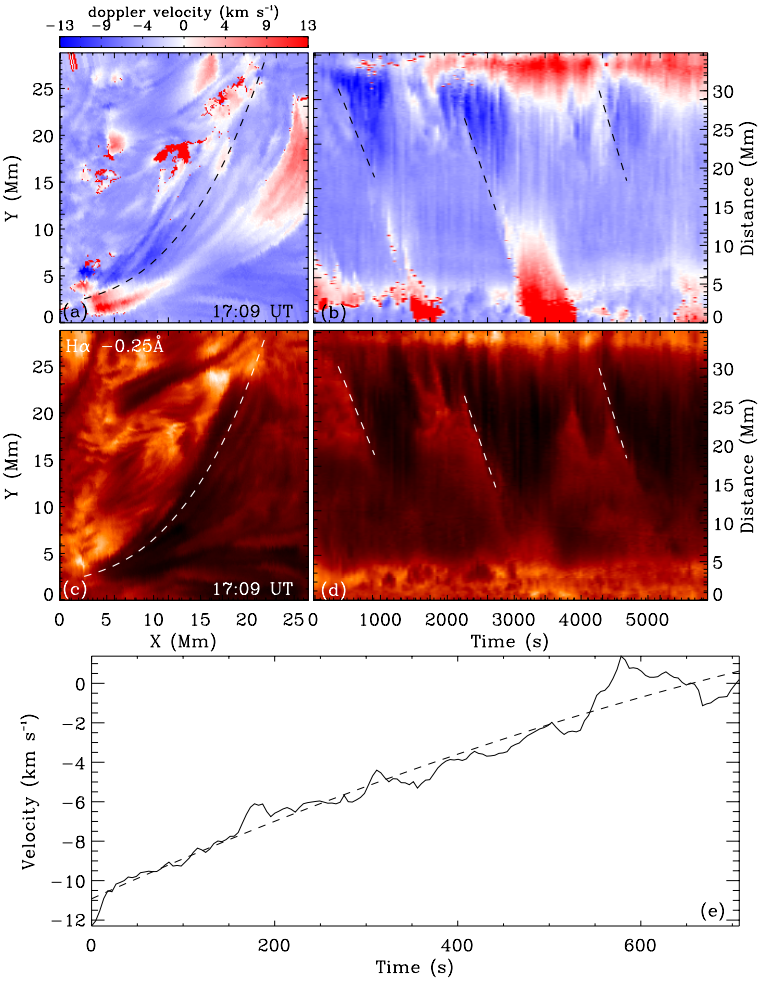

Fig. 4 Panels (a) and (c) exhibit the selected fibril used for calculating the time-distance map in Doppler velocity map and Hα image respectively. Panel (b) displays time evolution Doppler velocity of this slice and panel (d) is the time-distance map. Panel (e) depicts the Doppler velocity along one of the erupting fibrils.

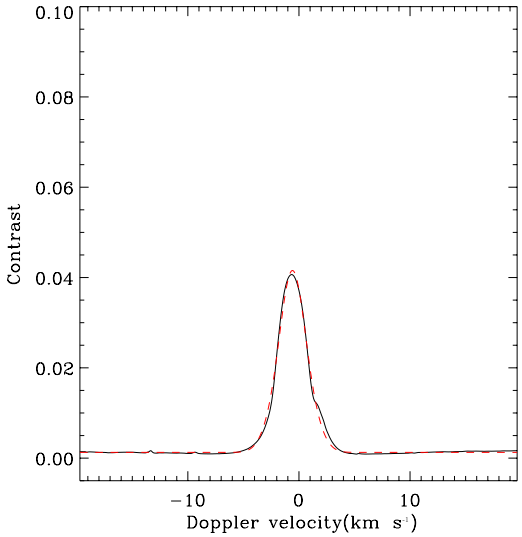

Fig. 5 Observed rms contrast profile (*black solid line*) and the fitting curve (*red dashed line*).

image panels in Figure 2. It can be seen that the footpoints of this surge are close to the positive parasitic magnetic poles embedded in the negative field. However, some parasitic magnetic poles are so weak (under 100 G) that they can hardly be identified in the figure. To illustrate the relationship between the magnetogram and the brightenings, we calculate the light curve of the brightenings and positive magnetic flux of the magnetogram (calculated from the red dashed boxes in Fig. 2). As we show in Figure 3, the magnetic flux curve exhibits a similar trend with the light curve. We note that there are some obvious peaks, which manifest similar peaks in magnetic flux that can be seen in the light curve, i.e., the double peaks from 16:31 UT to 16:40 UT in the light curve and the similar double peaks from 16:27 UT to 16:37 UT in magnetic flux. Moreover, the fluctuation from 16:58 UT to 17:10 UT in the light curve has a similar fluctuation in magnetic flux from 16:54 UT to 17:06 UT as well. In addition, a common point can be seen in both these two time periods, i.e., the magnetic flux increases are both four minutes before the increases of the light curve. The relations between the light curve and magnetic flux imply that the intensity enhancement in Hα is probably caused by the increasing photospheric magnetic flux. In all these phenomenons, the brightenings observed by chromospheric lines are co-spatial with the PIL and the increasing intensity associated with increasing magnetic flux, indicating a local chromospheric reconnection (Isobe et al. 2007; Nelson et al. 2015; Hong et al. 2017).

3.2 Velocities of Surge

As we mentioned in Section 3, the erupting plasmas exhibit absorption in both EUV and typical chromospheric lines, thus they were recognized as chromospheric activity. Chromospheric ejections often have a lower eruptive velocity. We evaluate the velocity of this surge including both light-of-sight (LOS) velocity and transverse velocity, via spectral analysis and the time-distance method. The LOS velocity, as shown in the bottom row of Figure 2, is about 10 – 13 km s^{-1} for newly formed fibrils and has a rapidly decreasing trend along the erupted fibrils. After 16:42 UT, the plasma that drops back dominates the area near footpoints. To evaluate the transverse velocity, a time-distance slice of a typical ejective fibril is displayed in Figure 4, panel d, which demonstrates that the speed is about 21 – 28 km s^{-1}. We further evaluate acceleration in the LOS direction. To evaluate the acceleration, we select one fibril (the same fibril as the one selected for calculating transverse velocity) and calculate its time evolution Doppler velocity map (Fig. 4b). Obviously, some eruption processes can be seen in both the time evolution Doppler velocity map and time-distance map. Based on the time evolution Doppler velocity map, the Doppler velocity evolution of eruption frontiers are selected frame by frame and are exhibited in Figure 4, panel e. The evolution curve gives an acceleration of –0.017 km s^{-2}. This acceleration is comparable with the value observed in filament downflow motion (Chae et al. 2008).

3.3 Cloud Model

The chromospheric spectral inversion can provide information on a local region or the whole chromosphere. In order to invert the spectrum, Beckers (1964) proposed a simple method named Beckers' cloud model (BCM). Their method is useful for evaluating the properties of objects above the chromosphere, such as filaments. However, in our observation, the local heating is embedded in the chro-

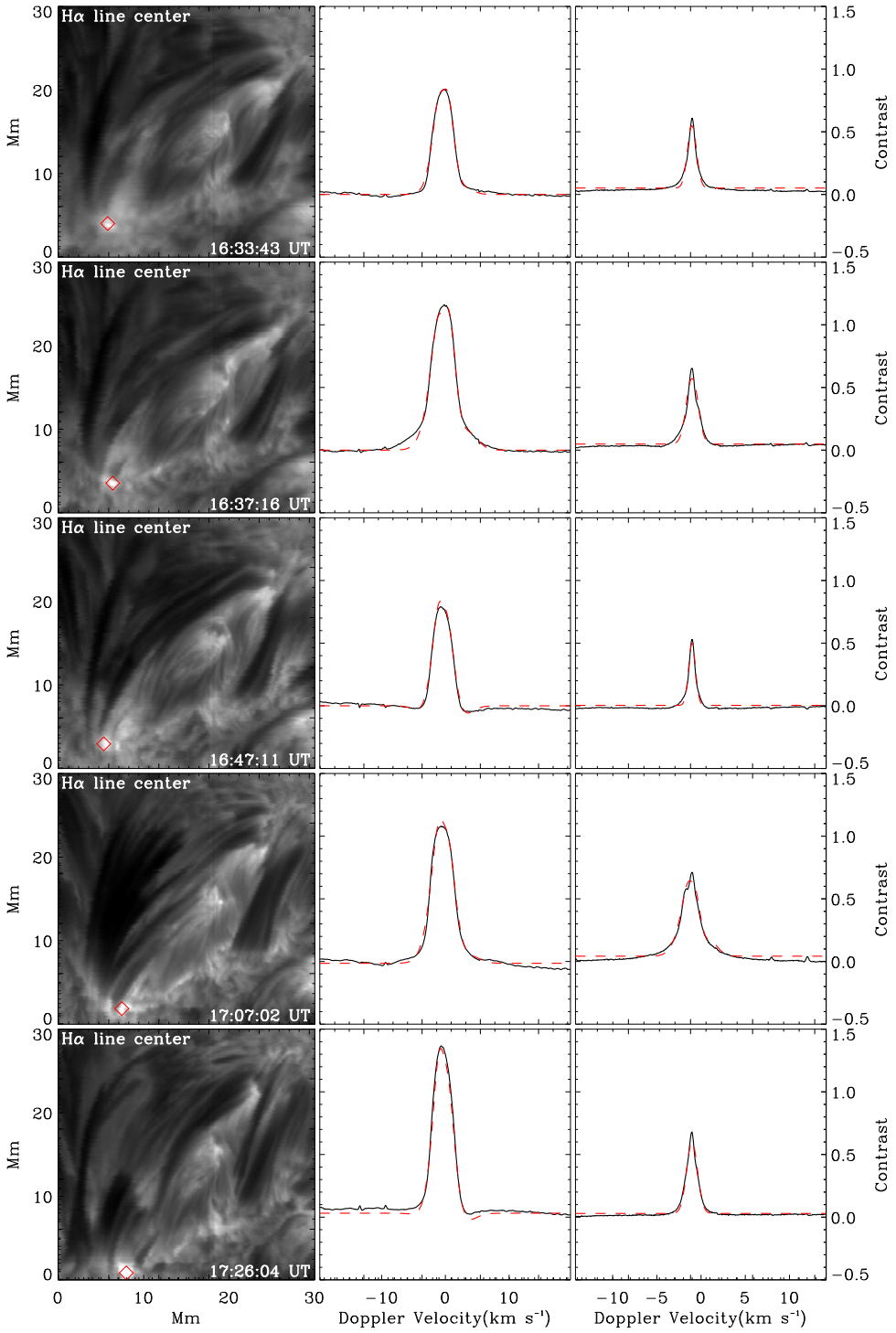

Fig. 6 The first column displays the positions of selected brightenings (*red quadrangles*). The second column shows the Hα line profiles (*black solid lines*) and fitting curves (*red dashed lines*). The third column depicts the Ca II line profiles and fitting curves in the same way as the Hα line.

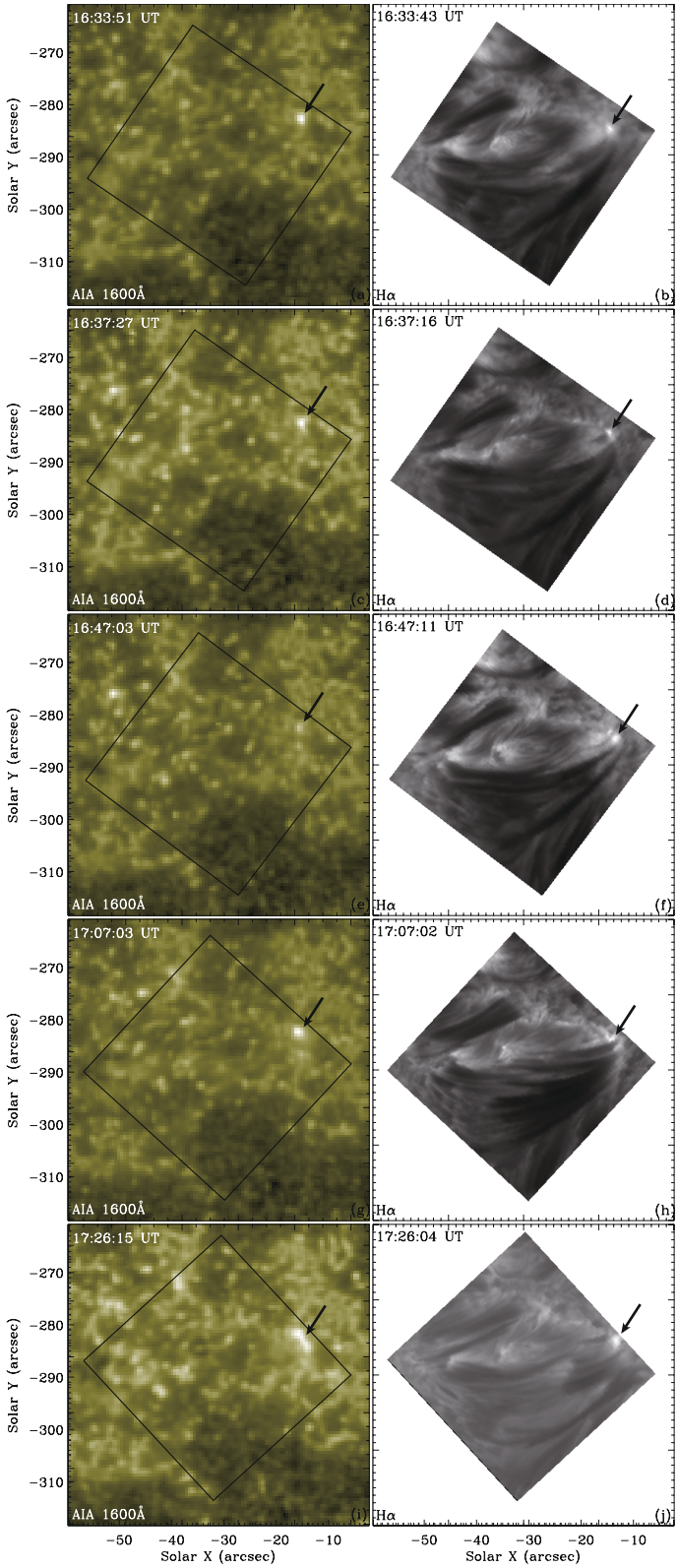

Fig. 7 Comparison of the 1600 Å images and Hα line center images. The left column is 1600 Å images and the right column is Hα. The *black quadrangles* signify the FOV of FISS/GST at different times, respectively. *Black arrows* indicate the bright point in 1600 Å and Hα images.

mosphere. For considering the embedded objects, Chae (2014) improved their method, namely the embedding cloud method, and extracted some useful information from their FISS data. Furthermore, using this method, Hong et al. (2014) also calculated the temperature of an Ellerman bomb from the Hα line observed by FISS, which is similar to the results of Fang et al. (2006) via semi-empirical modeling.

In BCM, the contrast profile can be described as follows

$$C_\lambda = \left(\frac{S}{I_{\lambda,\mathrm{in}}} - 1 \right) \left[1 - \exp\left(-\tau_\lambda \right) \right] \ , \tag{1}$$

where C_λ is the contrast profile, S is the source function of a calculated cloud, $I_{\lambda,\mathrm{in}}$ is an incident ray determined by observation of quiescent area $I_{\lambda,\mathrm{in}} = R_{\lambda,\mathrm{obs}}$ and τ_λ is the optical thickness of the cloud derived from the following equation

$$\tau_\lambda = \tau_0 \exp\left[- \left(\frac{\lambda - \lambda_1}{W} \right)^2 \right] \ . \tag{2}$$

Here τ_0 is the optical thickness of the line center, λ_1 is the Doppler velocity of the cloud and W is the Doppler width. According to Equation (1), the equation has four free parameters: S, τ_0, λ_1 and W. When the cloud is considered to be embedded, then the contrast profile can be derived from the following equation

$$\begin{aligned} C_\lambda = & \left(\frac{s}{R_{\lambda,\mathrm{obs}}} - 1 \right) \left[1 - \exp\left(t_\lambda - \tau_\lambda \right) \right] \\ & + \left[1 - \exp\left(-\tau_\lambda \right) \right] \frac{S - s}{R_{\lambda,\mathrm{obs}}} \ . \end{aligned} \tag{3}$$

Some new parameters can now be included, where s is the ensemble-average of S and t_λ is the optical thickness of the reference area derived by the equation as follows

$$t_\lambda = t_0 \exp\left[- \left(\frac{\lambda - \lambda_2}{w} \right)^2 \right] \tag{4}$$

with the three new parameters: t_0, λ_2 and w.

According to Equation (3), eight parameters are needed for fitting the contrast profile of target objects. To reduce the number of free parameters, the method mentioned in the appendix of Chae (2014) is applied for fixing four parameters: s, λ_2, ω and t_0. The root mean squared (rms) contrast profile G_λ and its fitting curve are displayed in Figure 5. According to the assumption of complete frequency redistribution, the source function for Hα is calculated as follows

$$S_\lambda = \frac{2hc^2}{\lambda^5} \frac{1}{\frac{b_2}{b_3} \exp\left(\frac{hc}{\lambda k T} \right) - 1} \ . \tag{5}$$

In this equation, λ is the wavelength of Hα, the h, k and c are Planck constant, Boltzmann constant and speed of light respectively, b_2 and b_3 are departure coefficients of a hydrogen atom at energy levels 2 and 3 respectively and T is the local temperature. Since the contrast profiles exhibit a single peak, the main heating is concentrated in the Hα line center. Thus we chose the heated layer with a height range from 1900 km to 2100 km. The values of b_2, b_3 and T will be chosen from the VAL C model. To evaluate the source function of heated footpoints, we select five typical brightenings and assigned them in Figure 3. They are all peaks of intensity enhancement shown in Figure 3. The positions (first column), Hα contrast profiles and fitting curves (second column), and Ca II profiles and fitting curves (third column) of bright points are displayed in Figure 6. Based on the fitting parameters, the relative increase of source function and increased temperature are listed in Table 1. The increase of temperature is about 800 K to 3500 K, which means a heating up to 8 kK – 13 kK. This result is a bit lower than the inversion of Robustini et al. (2018), namely 14 kK. Furthermore, in their study, the intensity enhancement is co-spatial with the 1600 Å brightening. Thus, they suggest that the local heating may heat the footpoint up to a higher temperature and the Ca II based inversion is insensitive to temperature above 15 kK because the Ca II is ionized. In contrast, we display a comparison of the Hα images and 1600 Å images in Figure 7. As we show in these figures, the brightenings in 1600 Å are not co-spatial with the Hα one until 17:26 UT. A few minutes after this time, the footpoints of the surge exceed our FOV and thus further situations are unknown.

4 DISCUSSION AND CONCLUSIONS

Our study is based on the analysis of a fan-shaped surge in NOAA Active Region 12401 and we have been able to obtain its properties: the surge has a transverse velocity of about 23 – 28 km s^{-1} and an initial LOS velocity of about 11 – 13 km s^{-1}. The eruptive fibrils are associated with the footpoint brightenings after the increase of magnetic flux. Thus, the most probable trigger mechanism of the surge is magnetic reconnection. The surge is absorptive in both chromospheric lines and EUVs. Hence the erupting plasma should be cold and dense, which means that this reconnection occurs in the chromosphere.

Plasma heating via chromospheric reconnection has been discussed for decades, but it is still unclear whether plasma can be heated up to tens of thousands of Kelvin. In previous works, some authors suggested that the chromospheric brightenings caused by reconnection can be co-spatial with some ultraviolet (UV) and EUV brightenings, such as *IRIS* bombs (Vissers et al. 2013; Tian et al. 2016). However, as we mentioned in Section 3.3, no EUV or UV brightenings are co-spatial with our observation from 16:22 UT to 17:26 UT (see the black arrows in Fig. 7).

During this period, our inversion of plasma temperature shows that the local plasma heating is weak. Thus, we suggest that in the first half of our observation period, our inversion from Hα line, namely 8 – 13 kK, is a reliable result.

The Hα surge and filament formation can be linked to each other by the injection scenario proposed by Chae (2003). They both undergo a process in which cool and dense materials erupt by chromospheric reconnection. The differences are that most surges erupt and materials flow along a magnetic arch without dips, thus they will drop back to the chromosphere. But if the mass flows through a magnetic tube with a dip, such as a filament channel, then it will stay in this dip and become filament mass. Some of the previous studies support this scenario (Liu et al. 2005; Zou et al. 2016, 2017; Wang et al. 2018). However, most of the reported filaments are active region filaments or intermediate filaments, which provide a strong magnetic environment for surges to replenish enough materials to sufficient height. But quiescent filaments have weaker magnetic environments and higher heights, so whether this scenario still works is doubtful.

The simulation by Jiang et al. (2011) found that the initial eruption of a surge is generated by the tension force of reconnection and the subsequent ascending motion is sustained by the pressure gradient force caused by plasma heating. Because of the weak magnetic field strength, the initial LOS velocity of our observation is about 11 – 13 km s^{-1}. In association with the local heating, the LOS velocity decreases with an acceleration of 0.017 km s^{-2} along the fibril (a resultant acceleration of gravity and pressure gradient force). As derived from the initial Doppler velocity and acceleration, the height of this surge is about 4800 km, which is lower than the typical active region filament height. This low height is due to two factors, the first is the acceleration and the second is the inclination angle of the magnetic field lines. Evaluating from the initial velocities of this surge, the inclination angle of this surge is 62°. Assuming that the magnetic tubes of this surge have smaller inclination angle, such as 50°, the plasma can be lifted up to about 10 Mm, which is the typical active region filament height. This means that even though the magnetic reconnection occurs in a weak magnetic field and causes a weak plasma heating, it can still replenish materials for active region filaments. Even if we assume that the magnetic tube is vertical, which means that the initial velocity against gravity is the resultant velocity of this surge, e.g., 31 km s^{-1}, the maximum height derived from this velocity and acceleration is 26 Mm. Consequently, this surge can hardly replenish materials for those quiescent filaments with 25 Mm or even higher because the initial velocity caused by the weak magnetic field is too low. In particular, some footpoints of quiescent filaments are rooted in the weaker magnetic field. Thus, we think that the injection model does not work well in the formation of quiescent filaments.

Acknowledgements The authors are grateful to the referee for their useful comments. This work was supported by the National Natural Science Foundation of China (41731067 and 41822404), Shenzhen Technology Project (JCYJ20170307150645407) and the Fundamental Research Funds for the Central Universities (Grant No. HIT.BRETV.201901). P. Z. also acknowledges the support by China Postdoctoral Science Foundation (2018M641812). W. C. acknowledges support of the US NSF (AGS-1821294) and the National Natural Science Foundation of China (11729301). The BBSO operation is supported by NJIT and US NSF AGS 1821294 grant. The GST operation is partly supported by the Korea Astronomy and Space Science Institute and Seoul National University, and by the strategic priority research program of Chinese Academy of Science (CAS) (Grant No. XDB09000000).

References

Antiochos, S. K., & Klimchuk, J. A. 1991, ApJ, 378, 372
Asai, A., Ishii, T. T., & Kurokawa, H. 2001, ApJ, 555, L65
Beckers, J. M. 1964, A Study of the Fine Structures in the Solar Chromosphere, PhD thesis, Sacramento Peak Observatory, Air Force Cambridge Research Laboratories, Mass., USA
Cao, W., Gorceix, N., Coulter, R., et al. 2010, Astronomische Nachrichten, 331, 636
Chae, J. 2003, ApJ, 584, 1084
Chae, J. 2014, ApJ, 780, 109
Chae, J., Ahn, K., Lim, E.-K., Choe, G. S., & Sakurai, T. 2008, ApJ, 689, L73
Chae, J., Park, H.-M., Ahn, K., et al. 2013, Sol. Phys., 288, 1
Chen, P. F. 2011, Living Reviews in Solar Physics, 8, 1
Dahlburg, R. B., Antiochos, S. K., & Klimchuk, J. A. 1998, ApJ, 495, 485
Deng, Y. Y., Schmieder, B., Engvold, O., DeLuca, E., & Golub, L. 2000, Sol. Phys., 195, 347
Fang, C., Tang, Y. H., Xu, Z., Ding, M. D., & Chen, P. F. 2006, ApJ, 643, 1325
Goode, P. R., & Cao, W. 2012, in Proc. SPIE, Vol. 8444, Ground-based and Airborne Telescopes IV, 844403
Hong, J., Ding, M. D., Li, Y., Fang, C., & Cao, W. 2014, ApJ, 792, 13
Hong, J., Ding, M. D., & Cao, W. 2017, ApJ, 838, 101
Hou, Y. J., Li, T., Yang, S. H., & Zhang, J. 2016, A&A, 589, L7
Isobe, H., Tripathi, D., & Archontis, V. 2007, ApJ, 657, L53
Jiang, R. L., Shibata, K., Isobe, H., & Fang, C. 2011, ApJ, 726, L16
Kippenhahn, R., & Schlüter, A. 1957, ZAp, 43, 36
Kuperus, M., & Raadu, M. A. 1974, A&A, 31, 189
Leake, J. E., & Linton, M. G. 2013, ApJ, 764, 54

Lemen, J. R., Title, A. M., Akin, D. J., et al. 2012, Sol. Phys., 275, 17
Li, T., & Zhang, J. 2016, A&A, 589, A114
Li, Z., Fang, C., Guo, Y., et al. 2016, ApJ, 826, 217
Liu, Y., Kurokawa, H., & Shibata, K. 2005, ApJ, 631, L93
Mok, Y., Drake, J. F., Schnack, D. D., & van Hoven, G. 1990, ApJ, 359, 228
Nelson, C. J., Scullion, E. M., Doyle, J. G., Freij, N., & Erdélyi, R. 2015, ApJ, 798, 19
Okamoto, T. J., Tsuneta, S., Lites, B. W., et al. 2008, ApJ, 673, L215
Robustini, C., Leenaarts, J., & de la Cruz Rodríguez, J. 2018, A&A, 609, A14
Robustini, C., Leenaarts, J., de la Cruz Rodriguez, J., & Rouppe van der Voort, L. 2016, A&A, 590, A57
Roy, J.-R. 1973, Sol. Phys., 32, 139
Rust, D. M., & Kumar, A. 1994, Sol. Phys., 155, 69
Scherrer, P. H., Schou, J., Bush, R. I., et al. 2012, Sol. Phys., 275, 207
Schou, J., Scherrer, P. H., Bush, R. I., et al. 2012, Sol. Phys., 275, 229
Shimizu, T., Katsukawa, Y., Kubo, M., et al. 2009, ApJ, 696, L66
Song, H. Q., Cheng, X., Chen, Y., et al. 2017, ApJ, 848, 21
Tian, H., Xu, Z., He, J., & Madsen, C. 2016, ApJ, 824, 96
van Ballegooijen, A. A., & Martens, P. C. H. 1989, ApJ, 343, 971
Vissers, G. J. M., Rouppe van der Voort, L. H. M., & Rutten, R. J. 2013, ApJ, 774, 32
Wang, J., Yan, X., Qu, Z., et al. 2018, ApJ, 863, 180
Xia, C., & Keppens, R. 2016, ApJ, 823, 22
Xia, C., Keppens, R., & Guo, Y. 2014, ApJ, 780, 130
Yang, S., Zhang, J., & Erdélyi, R. 2016, ApJ, 833, L18
Zou, P., Fang, C., Chen, P. F., et al. 2016, ApJ, 831, 123
Zou, P., Fang, C., Chen, P. F., Yang, K., & Cao, W. 2017, ApJ, 836, 122